Journal of Materials Chemistry A

ROYAL SOCIETY OF CHEMISTRY

PAPER

View Article Online
View Journal | View Issue

Cite this: J. Mater. Chem. A, 2025, 13, 13354

High-performance aqueous sodium-ion storage using bundled fiber-based electrodes†

Mohan Reddy Pallavolu, ‡[a] Sateesh Panugamti,‡[b] Vishwanath Hiremath, [c] Bhargav Akkinepally, [b] Goli Nagaraju, *[d] Jaesool Shim*[b] and Sang Woo Joo*[b]

Fiber-based small-scale energy storage devices, enabling high energy density and power densities are highly desirable for miniatured portable electronic devices. However, fiber-based supercapacitors have limitations in terms of energy density owing to their small and slender electrode architectures. In this work, we design high-performance bundled fiber-type supercapacitors using sodium-ion pre-intercalated manganese oxide on carbon fiber bundles (Na–MnO_2@CFBs) and palmyra fruit-derived porous carbon array electrodes. We used the electrodeposition method to pre-intercalate Na-ions in the void spaces of MnO_2 layers and form core–shell-type nanoarchitectures, which are favorable in elevating electrochemical active sites and pseudocapacitive charges. Specifically, core–shell Na–MnO_2@CFBs electrodes provide higher Na-ion energy storage with a maximum specific capacitance of 222.5 F g^{-1} and a length capacitance of 13.3 mF cm^{-1} in aqueous sodium sulfate electrolyte. The core–shell Na–MnO_2@CFBs electrode also exhibits excellent electrochemical stability (95.6%) because of their hierarchical nanoarchitectures and good structural durability. Furthermore, the fabricated bundled fiber-type asymmetric supercapacitor exhibited high energy (18.04 W h kg^{-1}) and power (5829.1 W kg^{-1}) densities with good cycling stability. These results showed that bundled fiber electrodes and pre-intercalated alkali cations in MnO_2 layered structures could be employed as promising potential electrodes for small-scale energy storage applications to achieve high energy and power densities.

Received 3rd February 2025
Accepted 25th March 2025

DOI: 10.1039/d5ta00887e

rsc.li/materials-a

1. Introduction

Future portable electronic applications are driving innovation in energy storage technology, particularly with the increasing demand for small, slim supercapacitors (SCs) and Li-ion batteries that can power devices like wearable watches, health-care sensors, flexible electronics, micro-robots, and smart devices.[1–3] Among various energy storage devices, SCs have attracted widespread attention as an advanced energy storage system owing to their reliable safety, fast charging–discharging rates, long-cycling life, low-cost and high-power density.[4] Downsizing SCs into fiber-type and printed micro-sized devices with enhanced energy density has been considered a key feature of a technological revolution in electronic applications.[5–7] Carbon-based materials (activated carbon and reduced graphene oxide) are mainly used as capacitive-type double-layer electrode materials in symmetric SCs, considering their excellent cycling stability and high-power density but fail to achieve high energy density.[8] While pseudocapacitive SCs, also known as redox SCs, combine the mechanisms of non-Faradic double-layer charge storage with redox (oxidation–reduction) reactions. This unique combination enables pseudocapacitive materials (manganese oxide, ruthenium oxide, *etc.*) to achieve higher capacitance and energy storage performance.[9] However, the limitation of pseudocapacitors arises when there is a need to deliver high energy at high power levels. In such cases, the thickness of the active material layer becomes crucial, as the material is too thick, it can impede the rapid movement of ions and electrons, thus limiting the device ability to deliver high-energy storage efficiently.[10–12] Increasing the active material mass loading, and improving the energy storage properties together with extended cell voltage are highly desirable for practical electronic applications.[13] Accordingly, asymmetric SCs (ASCs) have been designed to exhibit higher energy density than symmetric SCs owing to their mixed energy storage mechanism, including capacitive- and redox-type electrode materials. To improve the cell voltage and energy density of fiber-type devices, rational design of capacitive- and metal oxide nanostructured materials are highly desirable, as the surface area and

[a]School of Chemical Engineering, Yeungnam University, Gyeongsan 38541, Republic of Korea

[b]School of Mechanical Engineering, Yeungnam University, Gyeongsan 38541, Republic of Korea. E-mail: jshim@ynu.ac.kr; swjoo@yu.ac.kr

[c]Department of Chemistry, Kishkinda University, Mount View Campus, Ballari, Karnataka 583104, India

[d]Department of Materials, Imperial College London, London SW7 2AZ, UK. E-mail: nagarajugoli7@gmail.com; n.goli@imperial.ac.uk

† Electronic supplementary information (ESI) available. See DOI: https://doi.org/10.1039/d5ta00887e

‡ M. R. P and S. P equally contributed to this work.

electroactivity are key properties to enrich the adsorption/desorption and redox reaction process.[14]

The design of advanced electrode materials for supercapacitors (SCs) has been extensively studied to enhance energy storage performance. The precise engineering of anode and cathode materials at the nanoscale plays a crucial role in optimizing energy storage properties.[15] Recently, layered manganese oxide (MnO_2) has garnered more attention owing to their high surface area, rich valency states, favorable electrochemical properties, abundance, and low cost.[16,17] Moreover, MnO_2 showed pseudocapacitance due to the faradaic reactions during charge and discharge cycles, which ensure to delivery of higher electrochemical performance than capacitive materials. The pre-intercalation of alkali-metal ions in the layered structure of MnO_2 further implies much higher capacitance, which is favorable for high-energy-density asymmetric SCs. After the pre-intercalation of alkali ions (Li^+, Na^+, K^+), the layered structure of MnO_2 is expanded, which facilitates facile impregnation of electrolyte ions, enables efficient change transfer, and controlled redox kinetics.[18] Accordingly, the alkali intercalated MnO_2 could be considered as a potential electrode material owing to their high electrochemical performance with improved cycling stability. Recently, Na–MnO_2 has been demonstrated in a variety of morphologies and applications, including nanorods and needle-like structures for SCs and Na-ion battery applications, respectively.[19] The layered intercalation structure and strong Na cation dispersion of Na_xMnO_2 make them electrochemically desirable for energy storage devices.[20] For example, Sheng Liu *et al.*[21] demonstrated $Na_2Mn_5O_{10}$ for SCs, which revealed a maximum specific capacitance of 178 F g^{-1} at 0.1 A g^{-1} current density. More recently, Radhiyah *et al.*,[22] reported that nanoflake-like Na–MnO_2 showed a high capacitance of 200 F g^{-1} in 1 M Na_2SO_4 electrolyte. However, to use it as an efficient pseudocapacitive electrode, the energy storage performance of the pre-intercalated MnO_2 needs to be further improved by tailoring the morphology and binder-free growth.

Meanwhile, the design of miniaturized fiber-type SCs relies on flexible current collectors, which include conductive fiber or wire-shaped electrodes (nickel wire, copper fiber, carbon fiber, and reduced graphene oxide yarn) and they were widely reported for wearable energy storage devices.[23] The energy storage performance of these fiber-type SCs was analyzed by growing various metal oxides, and carbon materials and demonstrated their applications by illumination of light-emitting diodes and portable electronic screens. However, these fiber-type devices use solitary fiber current collectors, which limits the energy storage performance owing to the poor surface area and low accessible electrode material loading.[24] Recently, Liu *et al.* reported Ni-coated yarns *via* $(NH_4)_2PdCl_4$ activation and Ni plating approach for fiber-type SCs.[25] Handayani *et al.*, developed CNT yarns by a direct-spinning method of CNT stack sheets and used them for high-voltage fiber-type SCs.[26] Although the devices exhibited desirable performance, the methods used for the development of multi-fiber current collectors are expensive and time-consuming. Therefore, rational design of three-dimensional (3D) and interwoven fiber bundles is highly desirable to increase the mass loading and elevate the energy storage performance. Specifically, carbon fiber bundles (CFBs) obtained from the carbon cloth can be easily tailored and arranged in various configurations. In the CFBs, the void space between each carbon fiber is wider, which allows a high amount of active material loading and optimization of electrode architecture, resulting in superior electrochemical performance.[27] Moreover, CFBs are lightweight and flexible, resulting in the fabrication of lightweight and flexible energy storage devices suitable for wearable electronics and portable energy storage systems. Therefore, the development of binder-free synthesis of pre-intercalated Na–MnO_2 in combination with interwoven CFBs could be expected to offer higher electrochemical performance and reduce the charge transfer resistance.

In this work, we designed sodium-intercalated MnO_2 (Na–MnO_2) on interwoven CFBs with controlled morphological features as a pseudocapacitive electrode using a simple electrochemical deposition method. During the growth process, the Na^+ ions intercalated on the surface of a layered structure of MnO_2, which initiates in the heterostructured (nanosheets on nanoflake) nanostructures of Na–MnO_2 on CFBs. Without the Na^+ ions intercalation, the dense or film-like growth of MnO_2 was obtained, which does not provide favorable electrochemical properties owing to the limited electrolyte accessibility and poor ion diffusion channels. The resulting heterostructured Na–MnO_2@CFBs showed two-fold enhanced specific capacitance compared to the pristine MnO_2 with a high potential window of 1 V owing to the enhanced electrochemical kinetics and improved charge storage properties. Moreover, the palmyra fruit-derived activated carbon (PFAC) was prepared using a simple pyrolysis method and used as a negative fiber-type electrode, which showed graphitic amorphous carbon with double-layer capacitive properties. Finally, fiber-type asymmetric SC (ASC) was fabricated using the Na–MnO_2@CFB as a positive electrode and PFAC@CFB as a negative electrode, which showed a cell voltage of 2.0 V with superior energy and power densities.

2. Experimental section

2.1. Synthesis of heterostructured sodium-intercalated manganese oxide on carbon fiber bundles (Na–MnO_2@CFBs)

Core–shell heterostructured Na–MnO_2 was synthesized by a simple and rapid electrodeposition technique at room temperature (RT). Initially, a set of carbon fiber bundles (CFBs) with a length of 5 cm were carefully peeled out from the carbon cloth (MTI Korea). The CFBs were then immersed in the nitric acid–sulfuric acid mixture (3 : 1) at 60 °C/3 h to improve the hydrophilic nature and washed with plenty of de-ionized water (DI-water) and ethanol, respectively. The dried CFBs were directly used as working electrode for the electrodeposition process. The growth solution was prepared by dissolving 20 mM of manganese acetate (Sigma Aldrich, South Korea) and 200 mM sodium sulfate (Na_2SO_4, Sigma Aldrich, South Korea) in 40 ml of DI water at RT. A three-electrode system comprised of CFBs as working, platinum (Pt) spring as counter, and Ag/AgCl as reference electrodes were immersed in the above growth

solution and applied a chronopotentiometry current of 1 mA for 10 min at RT. After the deposition, the brown color coating on CFBs was appeared, indicating the growth of the Na–MnO_2 layer on CFBs, which was washed with DI water and ethanol, respectively. The mass loading of Na–MnO_2 was estimated to be 0.34 mg on CFBs. The voltage response over the deposition time was recorded, as shown in Fig. S1(b).† Meanwhile, the dense morphology of MnO_2 was also prepared on CFBs under similar chronopotentiometry conditions without using Na_2SO_4 in the growth solution. The schematic presentation of Na-incorporated MnO_2 and pristine MnO_2 on CFBs is presented in Fig. 1(a). The characterization details of the prepared samples are provided in the ESI file.†

2.2. Preparation of palmyra fruit waste derived activated carbon (PFAC)

The biomass waste (palmyra fruit waste) was collected from agriculture fields in Chittoor, Andhra Pradesh, India. The dried palmyra fruit waste (without seed) was washed with DI water, oven-dried at 70 °C/6 h, and then crushed into fine powder using a grinder. The palmyra fruit powder (10 g) was then soaked in aqueous KOH solution and stirred overnight at 80 °C/6 h. The dried impregnated palmyra fruit waste is subjected to pyrolysis at 900 °C/2 h under an inert atmosphere. During pyrolysis, the KOH reacts with the carbonaceous material of palmyra fruit waste, which results in the formation of porous activated carbon. The as-prepared PFAC was treated in 1 M HCl

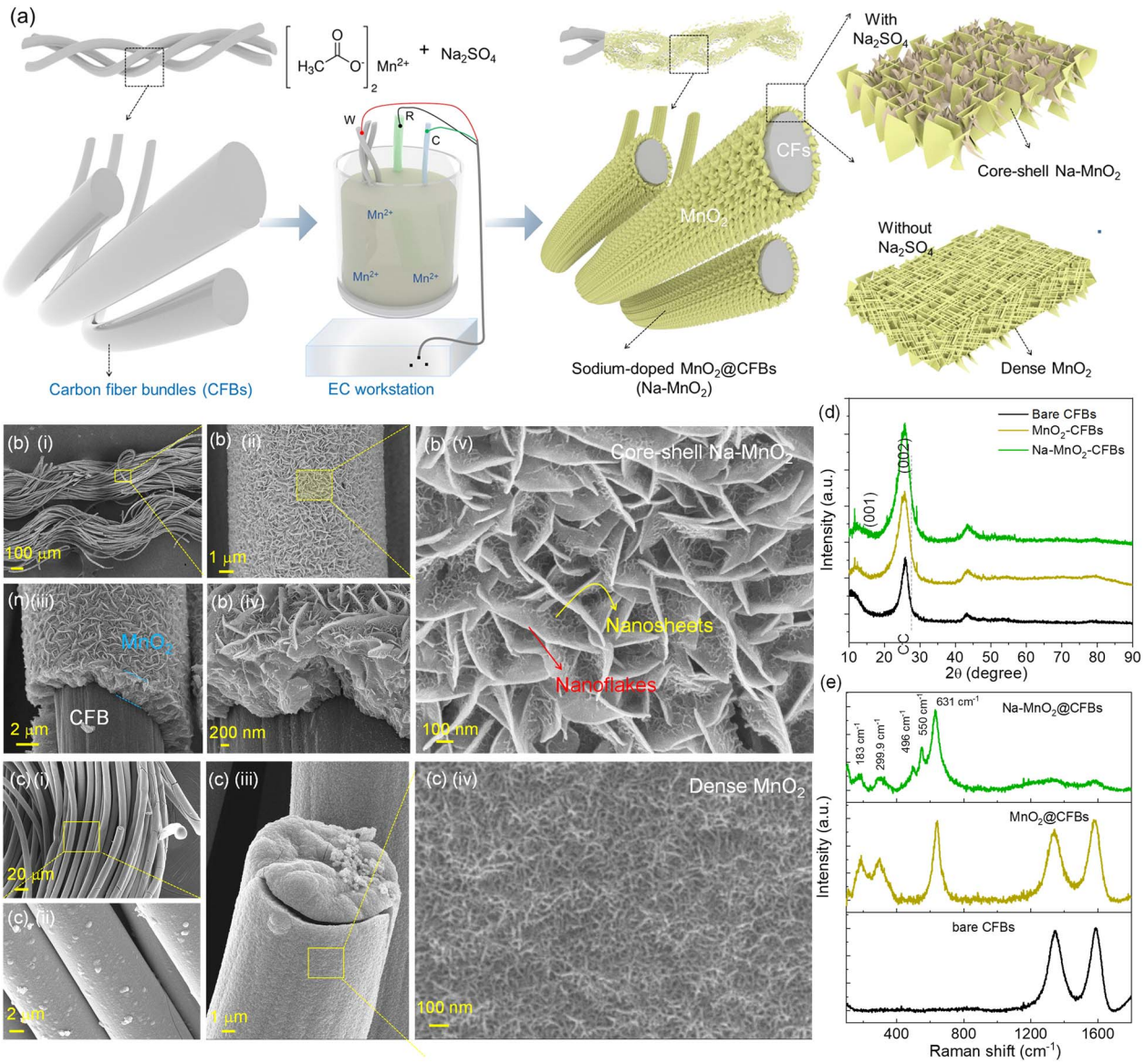

Fig. 1 (a) Schematic presentation of carbon fiber bundles (CFBs) and synthesis procedure for sodium incorporated core–shell Na–MnO_2@CFBs (with Na_2SO_4) and dense MnO_2@CFBs (without Na_2SO_4) by electrodeposition method. (b) (i–v) Low- and magnified SEM images of core–shell layered Na–MnO_2 on CFBs. (c) (i–iv) Low- and magnified SEM images of dense MnO_2 on CFBs obtained by Na_2SO_4-free growth solution. (d) XRD patterns and (e) HR-Raman spectra of bare CFBs, core–shell Na–MnO_2@CFBs and dense MnO_2@CFBs.

to remove the alkali impurities and washed with DI water and ethanol before drying in a hot oven overnight. Afterwords. PFAC was blended with polyvinylidene fluoride (PVDF) and carbon black with *N*-methyl pyrrolidone solvent. The blended slurry was cast on CFBs (with a length of 5 cm) to obtain PFAC@CFBs electrode and used for electrochemical characterizations. The characterization details of the prepared samples are provided in the ESI file.†

2.3. Fabrication of bundled fiber-type asymmetric SCs (ASCs)

The bundled fiber-type asymmetric ASC device was fabricated using core–shell Na–MnO_2@ CFBs as a positive electrode and PFAC@CFBs as a negative electrode. A non-woven wet wipe was used as a separator between both electrodes. Initially, an air-dried wipe paper was immersed in 1 M Na_2SO_4 electrolyte and twisted between the electrodes to mitigate the short circuit. The fiber-type device was then carefully wrapped by transparent parafilm (Parafilm®M), ensuring no leakage of the electrolyte. The fabricated fiber-type ASC device was then used for electrochemical properties.

3. Results and discussion

The morphological properties of the prepared samples were analyzed by scanning electron microscope, as presented in Fig. 1(b and c). Bundled and void-space-enhanced carbon fibers were evidenced in the low-magnification SEM image of Fig. 1(b)(i). After electrochemical deposition in manganese acetate and sodium sulfate solution, the smooth surface of the CFBs (Fig. S1(a)†) was uniformly covered with Na–MnO_2 nanostructures (Fig. 1(b)(ii)). The as-grown Na–MnO_2 heterostructures were vertically anchored on CFB with a strong binding property and a thickness of ~2.1 μm, as shown in the cross-sectional SEM images of Fig. 1(b)(iii and iv). Under the increased magnification, the SEM image of Na–MnO_2 showed numerous wrinkled nanosheets randomly distributed on nanoflakes, forming the core–shell-like heterostructures (Fig. S3†). Owing to the Na-ion intercalation in the layered structure of MnO_2, the deposited material manifest hierarchical nanoarchitectures with a core–shell-like morphologies. As shown in Fig. 1(b)(iv and v) and S3,† Na–MnO_2 consists of a hierarchical arrangement of deposited nanostructures with the core composed of lengthy nanoflakes that extend outward from the carbon fiber and surrounding the core, the shell consists of wrinkled nanosheets that are coated on the nanoflakes, forming a porous and interconnected Na–MnO_2 nanonetwork. The layered core–shell Na–MnO_2 on CFB with high void spaces in between the hierarchical nanoarchitectures could greatly facilitate the enhanced diffusion of electroactive ions and offer superior electrochemical performance.[28] On the contrary, a dense and compact film-like MnO_2 was grown on CFBs without using sodium sulfate (Na_2SO_4) in the growth solution. The dense MnO_2 grown on CFBs were included in the SEM images of Fig. 1(c)(i–iv). The morphological features reveal that the intercalation of Na-ions in the layered structure of MnO_2 plays a crucial role in engineering the shape and structural features of the prepared materials.[29,30] Fig. 1(d) shows the XRD patterns of bare fibers CFBs, dense MnO_2-deposited CFBs, and Na–MnO_2-deposited CFBs. The characteristic peaks of carbon at 24.8° and 44° of plane (002) and (004) belong to the bare carbon fibers. The diffraction peak with a weak intensity at 11.55° and 13.06° belongs to the tetragonal structure of α-MnO_2, which is consistent with the JCPDS No. 044-0141.[31] The low intensity of the active material appearing from the XRD patterns could be due to the low-mass loading or tiny electrode architectures. In addition, the α-MnO_2 crystal structure has 3-dimensional type 1 × 2 and 2 × 2 tunnels, which facilitate faster ion penetration and enhance the performance of electrode material for SCs. Furthermore, HR-Raman analysis was utilized to analyze the crystal structure of MnO_2 and Na–MnO_2 in detail. The Raman spectra of bare CC, MnO_2@CFBs, and Na–MnO_2@CFBs are presented in Fig. 1(e). From the Raman spectra, the characteristic bands at 1380 cm^{-1} and 1590 cm^{-1} belong to the D and G bands of carbon with an I_D/I_G ratio of 0.89, representing the higher degree of graphitization, and bands at 183, 299.9, 496, 550, and 631 cm^{-1} are characteristic signals for Na–MnO_2. The well-defined symmetric Mn–O signals of the Raman band at 631 cm^{-1} indicate well-developed tetragonal structure (2 × 2) tunnels in interstitial space.[32] The low-intense band at 183 cm^{-1} is attributed to the external vibration of the MnO_6 octahedral transition. The characteristic Raman bands for α-MnO_2 were associated with two major peaks at 631 cm^{-1} and 183 cm^{-1}.[32] These Raman results showed that the prepared samples were consistent with α-MnO_2, in line with the observations made by XRD analysis.

The morphological features of the core–shell Na–MnO_2 were further analyzed by using TEM and HR-TEM analysis. The TEM images in Fig. 2(a)(i and ii) show interconnected and void space-expanded Na–MnO_2 with stacked nanosheets-nanoflake architectures. We have also analysed the TEM images of MnO_2 (without Na intercalation), which shows the tiny nanosheet-like morphology (Fig. S2†). Additionally, the crystallinity of MnO_2 nanostructures without Na-ion intercalation is poor, as suggested by their weak lattice fringes in the crystal allignement of MnO_2 (Fig. S2(b)†). However, after Na-ion intercalation, layered distance between the multiple layers of Na–MnO_2 was increased with better crystallinity, as presented in HR-TEM image of Fig. 2(a)(iii). The designed heterostructured Na–MnO_2 with nanosheets-nanoflake could be expected to offer high conductivity and more active sites for pseudocapacitive energy storage in the electrolyte. Additionally, the nanoscale dimensions of these structures reduce the diffusion lengths for sodium and sulfate ions during charge and discharge processes. This can result in faster kinetics and higher rate capabilities, ultimately leading to improved capacitance and cycling stability, especially at high current densities. The elemental composition of Na–MnO_2 was further verified by the EDS analysis. Fig. 2(b) EDS spectrum and Fig. 2(c)(i–iv) line-scan mapping spectra confirm the presence of Mn, O, and Na elements in the prepared Na–MnO_2. While the EDS spectrum of MnO_2@CFBs (without Na-intercalation) only shows the characteristic elements of Mn, O, and C in the prepared sample (Fig. S1†). X-ray photoelectron

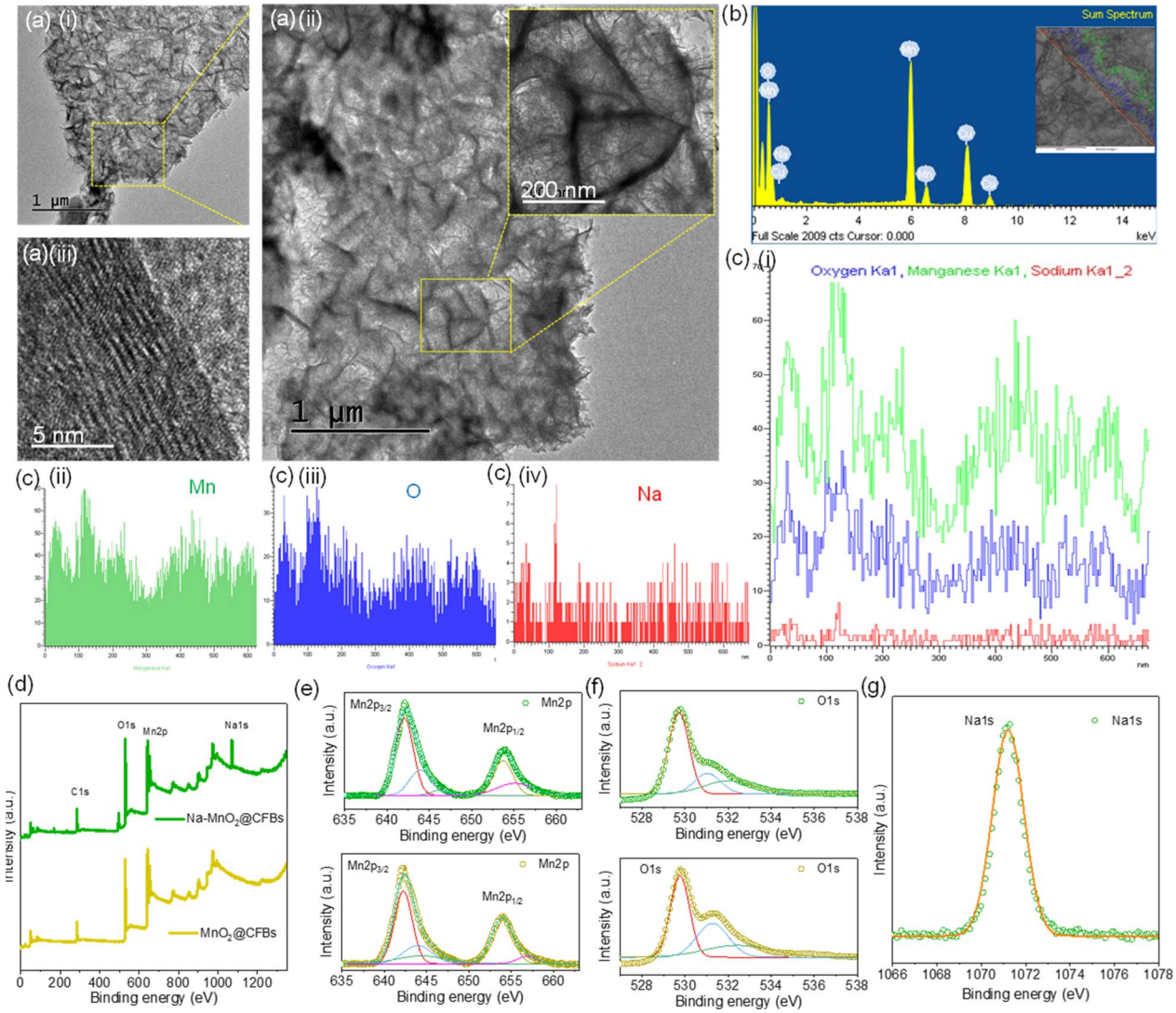

Fig. 2 (a) (i–iii) Low-, magnified TEM images and high-resolution TEM image of core–shell Na–MnO_2. (b) EDS spectrum of Na–MnO_2, and (c) (i–iv) overall elemental line-scan spectra, mapping line-scan of Mn, O and Na elements. (d) XPS survey scan spectra of dense MnO_2@CFBs and Na–MnO_2@CFBs. (e–g) High-resolution XPS spectra of Mn, O and Na elements in the prepared samples.

spectroscopy (XPS) is used to determine the valence states and elemental composition of the material. Fig. 2(d) shows the XPS survey spectra of dense MnO_2@CFBs and Na–MnO_2@CFBs, which shows the presence of Mn, O, Na, and C elements. The homogeneous distribution of elements is consistent with the line spectra of Na–MnO_2. Fig. 2(e) shows the high-resolution XPS spectra of Mn 2p of the dense MnO_2 and core–shell Na–MnO_2. The deconvoluted Mn $2p_{3/2}$ spectra of both samples showed 3 peaks that were centered at 642.1 eV, 643.7, 646.4 and 653.7, and 655.1 eV. The binding energy peaks at 642.1 and 653.7 eV were assigned to the Mn $2p_{3/2}$ and Mn $2p_{1/2}$ originated from Mn^{2+}/Mn^{3+} states, the binding energy values at 643.7 and 655.1 eV were assigned to the Mn^{4+} ionic state, respectively. Due to the similarities in their Mn $2p_{3/2}$ binding energies, it has been reported in the literature that the identification of Mn^{2+}, Mn^{3+}, and Mn^{4+} corroborated the binding energies of Mn $2p_{3/2}$ and Mn $2p_{1/2}$ core levels.[33] Furthermore, the peak intensity area under the curve of Mn^{3+} is higher than the Mn^{4+} state, indicating that Na^+ ion intercalation into the MnO_2 structure. Fig. 2(f) shows the high-resolution XPS spectra of O 1s, which shows the characteristics peaks at 529.7, 530.9, and 531.9 eV, indicating the metal–oxygen bond formation. The Na 1s XPS spectra in Fig. 2(g) show a highly intense peak at 1071 eV, indicating that the Na^+ ions effectively intercalate into MnO_2 structure and stabilize the structure within the center of 2 × 2 tunnels of the Na–MnO_2 crystal structure.[34]

The pre-intercalated core–shell Na–MnO_2@CFBs and bare MnO_2@CFBs electrodes were electrochemically tested in a three-electrode system to investigate their electrochemical performance. Using 1 M Na_2SO_4 as the electrolyte, Ag/AgCl as a reference electrode, and platinum mesh as a counter electrode, electrochemical studies were conducted at RT. The comparative cyclic voltammetry (CV) plots of dense MnO_2@CFBs and core–shell Na–MnO_2@CFBs measured at a scan rate

of 30 mV s^{-1} in the potential range of 0 to 1.0 V were presented in Fig. 3(a). From the comparative CV curves, it is evident that the area under the CV curve of Na–MnO_2 is higher than the pristine MnO_2. The quasi-redox shape of the MnO_2 and Na–MnO_2 confirms the pseudocapacitive behavior of the electrode material due to the rapid redox reactions of Na^+ ions in the MnO_2 interlayers.[22] Fig. 3(b) shows the comparative galvanic charge–discharge (GCD) curves for MnO_2 and core–shell Na–MnO_2 at a current density of 0.5 mA. The higher discharge time for core–shell Na–MnO_2@CFBs electrode indicates that it has higher specific capacitance than the pristine MnO_2@CFBs. The high capacitance could be ascribed the hierarchical nano-architectures and Na-ion pre-intercalation in the core–shell Na–MnO_2@CFBs electrode, which resulted in higher electroactivity and electronic conductivity. Fig. 3(c)(i) shows the calculated specific capacitance and length capacitance (Fig. 3(c)(ii)) values of MnO_2@CFBs and $NaMnO_2$@CFBs, which exhibited the capacitance of 221 F g^{-1} (20 mF cm^{-1}) and 130 F g^{-1} (10 mF cm^{-1}), respectively. The CV and GCD measurements were conducted at different scan rates of 10–100 mV s^{-1} and current ranges of 0.3 mA to 4 mA on core–shell Na–MnO_2@CFBs were evaluated to understand the electrochemical kinetics, reversibility, and rate performance as shown in Fig. 3(d and e). Upon increasing the scan rates, the CV curves of Na–MnO_2@CFBs showed increased peak currents due to shorter timescale for pseudocapacitive electrochemical reactions, while under slower scan rates, Na–MnO_2@CFBs led to lower peak currents. The shape of the CV curves was preserved even under high scan rates, indicating the good reversibility and electrochemical kinetics of the material. A similar redox behavior with

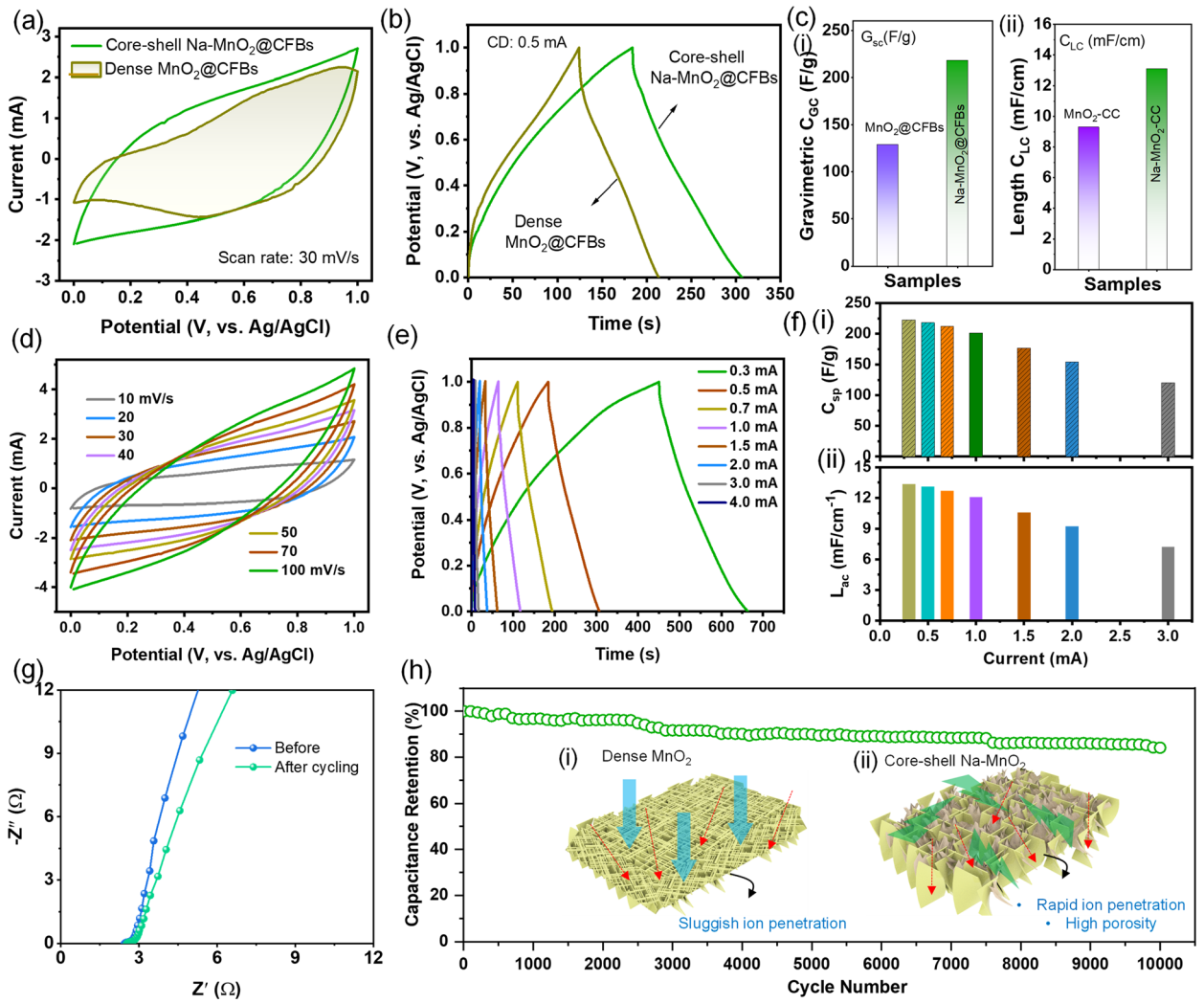

Fig. 3 Electrochemical properties of dense MnO_2@CFBs and Na–MnO_2@CFBs measured in a three-electrode system using 1 M Na_2SO_4 electrolyte. Comparative (a) CV profiles measured at a scan rate of 30 mV s^{-1}, (b) GCD curves measured at a charge–discharge current of 0.5 mA and (c) calculated gravimetric specific capacitance and length capacitance values of dense MnO_2@CFBs and Na–MnO_2@CFBs. (d) CV curves at different scan rates of 10–100 mV s^{-1} and (e) GCD profiles recorded at various charge–discharge currents of 0.5–4.0 mA, (f) (i) specific capacitance and (f) (ii) length capacitance values of Na–MnO_2@CFBs electrode. (g) Nyquist plots before and after cycling stability and (h) long-term cycling stability of Na–MnO_2@CFBs electrode. The inset in (g)(i) and (ii) shows the schematic diagram of MnO_2@CFBs and Na–MnO_2@CFBs electrodes during the ion penetration and electrochemical process.

electrochemical kinetics was observed in dense MnO_2@CFBs but with lower current response and charge–discharge times (Fig. S4†). As illustrated in Fig. 3(e), the GCD profiles with unique charge–discharge behavior under varied current densities of 0.3 to 4 mA, confirms the stable charge storage response. Using the discharge profiles, the calculated specific capacitance and length capacitance under varied GCD currents of the core–shell Na–MnO_2@CFBs electrode were included in Fig. 3(f)(i and ii). At a discharge current of 0.3 mA, Na–MnO_2@CFBs showed a maximum specific capacitance of 222.5 F g^{-1} with a length capacitance of 13.3 mF cm^{-1}. Even at high discharge currents, the measured specific capacitance of Na–MnO_2@CFBs electrode was maintained to be 153.9 F g^{-1} (2 mA), 120.4 F g^{-1} (3 mA), 96.3 F g^{-1} (4 mA), affirming the high rate performance characteristics of Na–MnO_2@CFBs electrode. Based on these results, it can be inferred that Na–MnO_2 exhibits higher electrochemical energy storage performance than pristine MnO_2. Electrochemical behavior and charge transfer resistance of the core–shell Na–MnO_2@CFBs were evaluated by the electrochemical impedance spectroscopic (EIS) analysis. Fig. 3(g) shows the EIS plot of Na–MnO_2@CFBs before and after the cycling stability test. The core–shell Na–MnO_2@CFBs exhibited lower charge transfer resistance of 0.22 Ω and 0.4 Ω before and after the cycling tests. Because of the interconnected and numerous void spacing in the core–shell Na–MnO_2@CFBs, it shortens the ion diffusion and efficiently allows electrolyte ions to reach the Na–MnO_2@CFBs electrode surface. The long-life cycling stability test was conducted over 10 000 GCD cycles for the Na–MnO_2 electrode, as shown in Fig. 3(h). The continuous GCD tests revealed a capacitance retention of 84.1% after 10 000 cycles when tested at charge–discharge currents of 1.0 mA. Relatively low capacitance fading after a long-term cycling test proves the good stability of the Na–MnO_2@CFBs electrode and can be used as a potential positive electrode for the fabrication of asymmetric SCs. The schematic representation in the inset of Fig. 3(h)(i) and (ii), illustrates the electrolyte penetration and charge transportation between the two electrodes. The sluggish ion penetration on the dense structured MnO_2@CFBs and rapid ion penetration of high porosity core–shell Na–MnO_2@CFBs illustrate their structural merits towards better electrochemical performance. The core–shell Na–MnO_2@CFBs increase the electrode surface area and shorten the ionic conductive pathway towards elevated capacitance than the rigid/dense electrode architectured MnO_2@CFBs.

We have also demonstrated biomass waste-derived, cost-effective activated carbon electrode material using a simple pyrolysis process of dried palmyra fruits (borassus flabellifer). Fig. 4(a–c) shows the schematic representation of synthesis steps involved in the palmyra fruits-derived porous carbon (PFAC). For the preparation of cost-effective porous carbon, palmyra fruits as eco-friendly and abundantly available bio-waste in agricultural field was used. The palmyra fruits were collected from the local agricultural lands in Chittoor, Andhra Pradesh, India. The plant-based carbon materials are in high demand due to their low cost, eco-friendliness, easy availability, and sustainability. Palmyra fruit stands out as a valuable natural resource, with all parts of the tree offering various applications. The seed in the palmyra fruit was removed and the pulp was used for the preparation of porous carbon. The dried palmyra fruit pulp was cut into small pieces and blended into the form of fine powder, followed by immersing in the KOH solution. The KOH-activated palmyra fruit waste was then transferred into the tube furnace and heated at 900 °C/2 h with the flow of nitrogen atmosphere. After cooling to room temperature, the activated carbon was washed with HCl, water, and ethanol, respectively. Due to the alkali activation, the biomass-derived PFAC reveals numerous pores within the carbon particle, as shown in the SEM images of Fig. 4(c). The X-ray diffraction (XRD) pattern of PFAC exhibits broad diffraction peaks (Fig. 4(d)(i)), characteristic of an amorphous carbon structure with some degree of graphitization. A prominent broad peak at ~23° (2θ degree) corresponds to the (002) plane of turbostratic carbon, indicating a disordered arrangement of graphene layers with short-range stacking order. The absence of sharp crystalline peaks confirms the lack of ordered graphite-like structure, which is typical for biomass-derived activated carbons. Additionally, a weaker and broader peak around 42.3° (2θ), associated with the (100) plane, suggests the presence of randomly oriented graphitic domains. The presence of the disordered carbon/amorphous nature of PFAC was confirmed by the Raman analysis. Fig. 4(d)(ii) shows the Raman spectra of PFAC, which exhibit the D band and G band at nearly 1345.8 and 1598 cm^{-1}, respectively.[35] These characteristic bands assess the lattice defects, disordered nature, low symmetry carbon structure (D band), and scattering characteristic peak of graphite (G band). The I_D/I_G ratio of the PFAC sample is 0.89, indicating a higher degree of graphitization.[36] The electrochemical properties of PFAC-coated CFBs were conducted in three-electrode systems to investigate their electrochemical behavior and energy storage performance. Fig. 4(e) shows the CV curves of PFAC@CFBs carried out at different scan rates from 10 to 100 mV s^{-1}. All the CV curves exhibited an almost rectangular shape in the potential range of 0 to −1 V, indicating the electric double-layer capacitive (EDLC) behavior of the carbon material. With the increase in scan rate, the area under the CV curves was increased with no redox peaks, revealing the capacitive-charge storage kinetics of PFAC@CFBs. Fig. 4(f) shows the GCD curves of PFAC at different current densities of 0.5 to 3 mA with a potential window of 0 to −1 V. The specific capacitance values were calculated from the discharge curves of GCD plots and the calculated specific capacitance values were shown in Fig. 4(g). At various current densities of 0.3, 0.5, 0.7, 1.0, 1.5, 2.0, and 3.0 mA, the specific capacitance values were estimated to be 145, 127.7, 119.5, 112.6, 109.1 and 105.3 F g^{-1}, respectively. Evidently, the PFAC electrode material shows a high-rate capability of 72.6%. The PFAC also showed higher/comparable electrochemical performance with various biomass precursors (Table S1†). Furthermore, long cycle stability of PFAC electrode material was tested for 10 000 GCD cycles, as shown in Fig. 4(h). Over 10 000 GCD cycles, capacitance retention of 95% was exhibited, indication high structural stability and long cycle durability.

To investigate the practical energy storage performance, a bundled fiber-type asymmetric supercapacitor device (ASC)

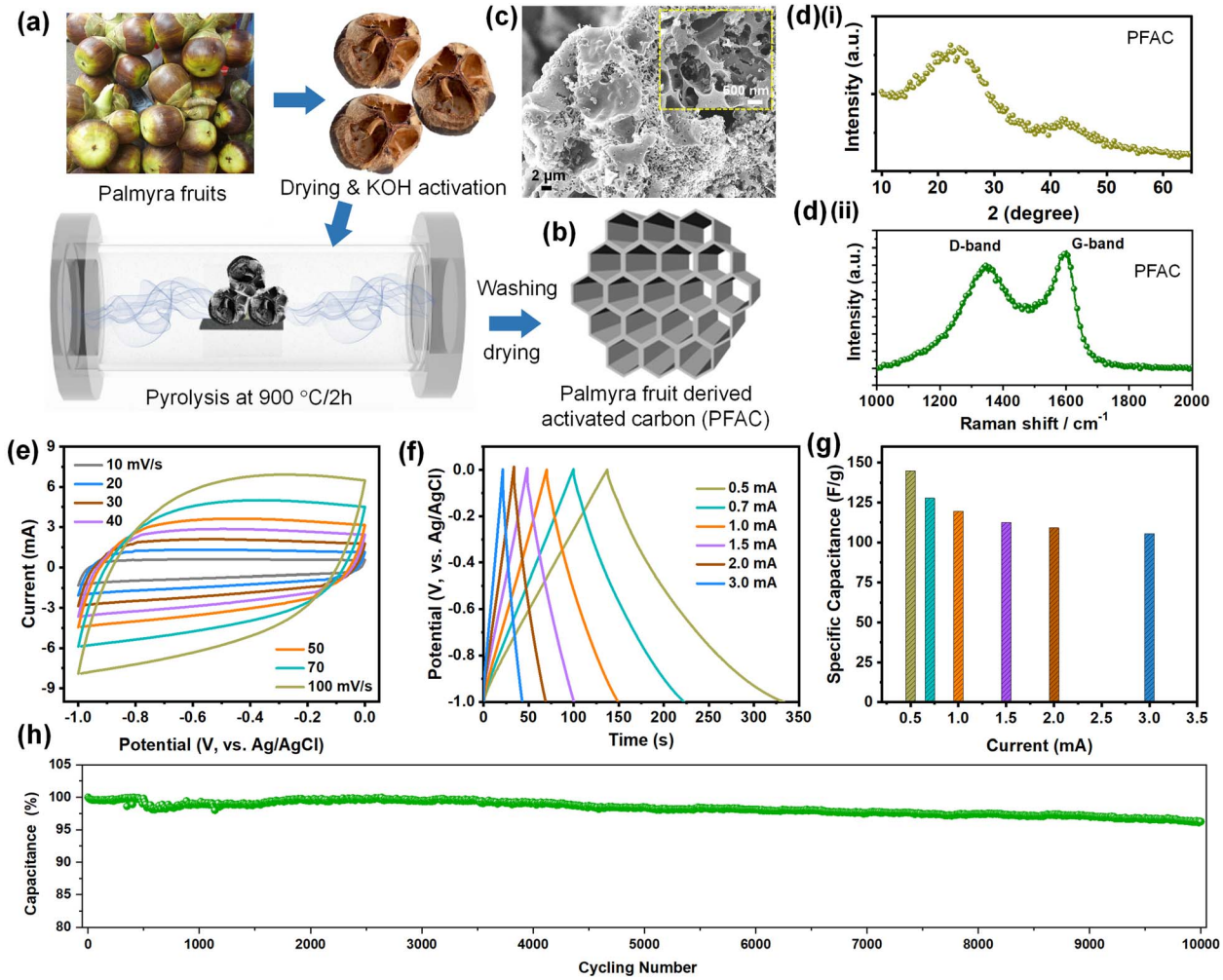

Fig. 4 Preparation process and electrochemical properties of biomass-derived PFAC@CFBs in three-electrode system at RT in 1 M Na_2SO_4 electrolyte. (a–c) Synthesis scheme and photographic images of palmyra fruits waste-derived highly porous activated carbon (PFAC) and SEM-images of the PFAC. (d) (i) XRD spectrum and (d) (ii) Raman spectrum of PFAC. (e–h) CV curves measured at varied scan rates of 10–100 mV s^{-1}, GCD curves under different charge–discharge currents of 0.5–3.0 mA, estimated gravimetric specific capacitance *vs.* discharge currents and cycling stability of PFAC@CFBs electrode.

was fabricated using PFAC@CFBs as negative electrode and Na–MnO_2@CFBs as positive electrode with Na_2SO_4 infiltrated wet wipe as separator at RT. The fabricated bundled fiber-type ASC device was schematically shown in Fig. 5(a). The photographic images of Na–MnO_2@CFBs and PFAC@CFBs electrodes and the fabrication process of bundled fiber-type ASC device were included in Fig. 5(b)(i–iv). Before assembling the Na–MnO_2@CFBs//PFAC@CFBs device, it is important to balance the mass and charges on both positive and negative electrodes. Accordingly, the individual electrochemical performance of Na–MnO_2@CFBs and PFAC@CFBs were separately measured in a three-electrode system. As presented in the CV (measured at a scan rate of 30 mV s^{-1}) and GCD curves (at 0.5 mA), the negative electrode was scanned between 0 to −1 V, and the positive electrode was scanned between the potential window of 0 to 1 V, respectively (Fig. 5(c and d)). Combining these two electrodes in the bundled fiber-type ASC, the device's working voltage window could be expected to be 2.0 V. From the measured electrochemical properties and using the mass balancing eqn (1), the mass ratio between the positive and negative electrodes was optimized.[37]

$$\frac{m^+}{m^-} = \frac{C_{ne}{}^- \times \Delta V^-}{C_{pe}{}^+ \times \Delta V^+} \quad (1)$$

where, m^+ is the mass (g), $C_{pe}{}^+$ is the specific capacitance (F g^{-1}) and ΔV^+ is the potential window (V) of the positive electrode, while and m^-, $C_{ne}{}^-$ and ΔV^- are the working mass, specific capacitance, and potential window (V) of the negative electrode, respectively. The optimized mass ratio (0.65) of positive to negative electrodes and to estimate the maximum working voltage ranges in bundled fiber-type ASC, electrochemical tests, including CV and GCD analysis were carried out. The CV profiles of fabricated ASC device at 30 mV s^{-1} scan rate and GCD profiles at 1 mA current density over various voltage ranges showed no discernible changes up to the potential window of 0–2 V, as shown in Fig. 5(e and f). Moreover, the ASC device

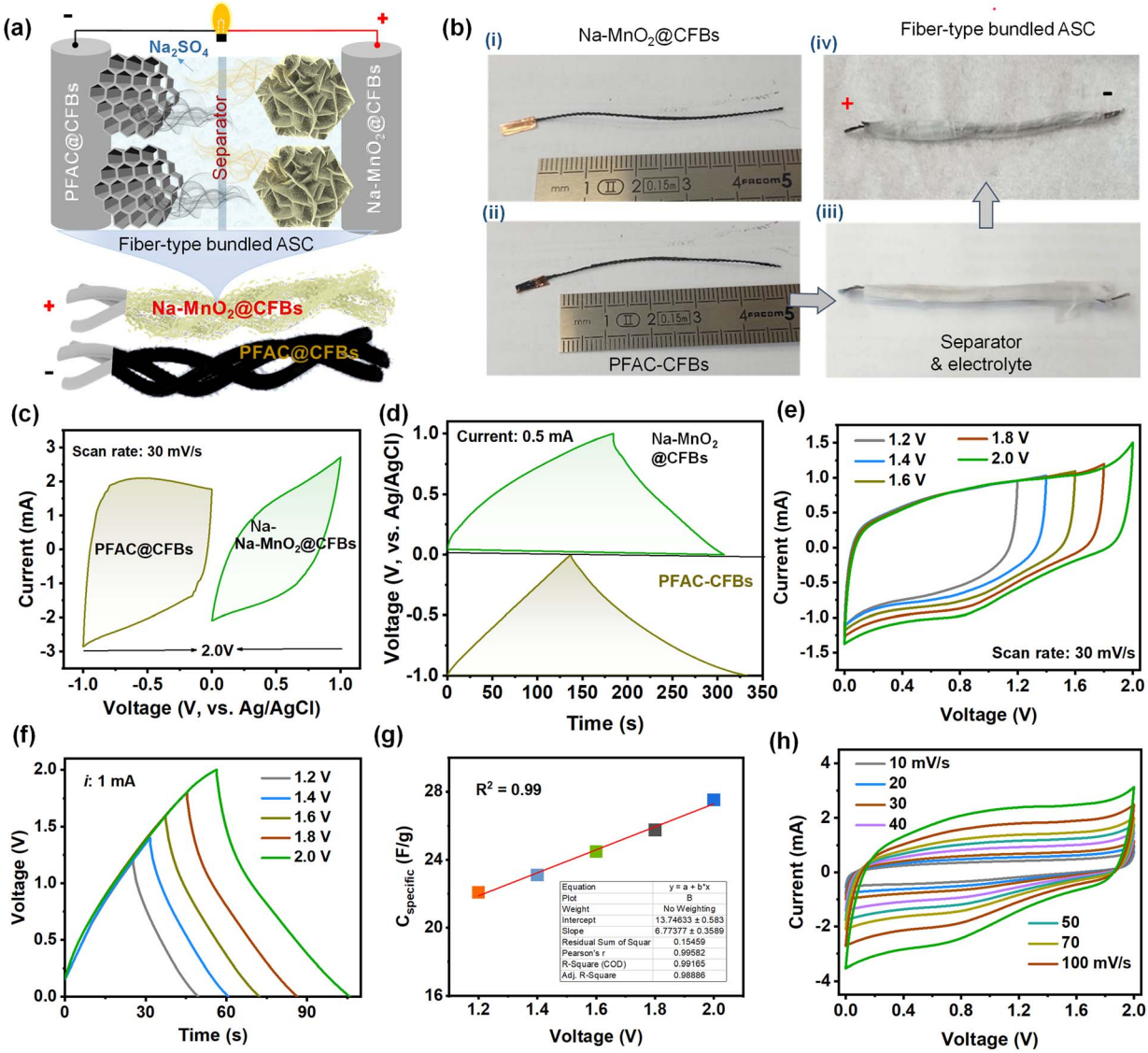

Fig. 5 (a) Schematic presentation and (b) (i–iv) fabrication process of bundled fiber-type ASC using core–shell Na–MnO_2@CFBs and biomass-derived PFAC@CFBs electrode. (c) CV curves (d) GCD curves of Na–MnO_2@CFBs and PFAC@CFBs electrodes measured in three-electrode system, which shows the expected voltage of 2.0 V after combining the two electrodes. (e) CV curves (f) GCD curves of the fabricated fiber-type ASC measured various working voltages 0–1.2 V to 0–2.0 V under constant scan rate and charge–discharge current, respectively. (g) Linear relationship capacitance response of the fabricated ASC upon increasing the device voltage and (h) CV curves of the corresponding device under various scan rates of 10–100 mV s^{-1} with the fixed working voltage of 0–2.0 V.

showed non-rectangular CV curves, suggesting a mixed charge contribution from the capacitive- and pseudocapacitive electrodes. Fig. 5(g) displays the calculated capacitance values within the various voltage ranges of 1.2, 1.4, 1.6, 1.8, and 2.0 V. Evidently, the specific capacitance increases with increasing voltage window and the specific capacitance follows the linear relationship (R^2 value of 0.99), which further affirms the good voltage stability without undergoing any undesirable side reactions. With the fixed voltage window of 0–2 V, the bundled fiber-type ASC was further tested at various scan rates of 10–100 mV s^{-1} (Fig. 5(h)) to investigate the electrochemical reversibility and electrochemical kinetics of the device. From the CV curves. Fiber-type devices showed capacitive- and pseudocapacitive redox response owing to the different charge storage materials without appreciable distortion in the CV shapes even as the scan rate climbs to a high scan rate of 100 mV s^{-1}.

Additionally, the GCD profiles of bundled fiber-type ASC devices were measured at various current densities of 0.5, 0.7, 1, 1.5, 2, 3, and 4 mA, to examine the specific capacitance and rate performance (Fig. 6(a)). GCD profiles with nearly symmetric forms indicate good coulombic efficiency. The specific capacitance values of bundled fiber-type ASC devices were calculated for various current densities and plotted in Fig. 6(b). Also, length capacitance that is the capacitance per unit length of an electrode, which is mostly expressed in unit of mF cm^{-1} was

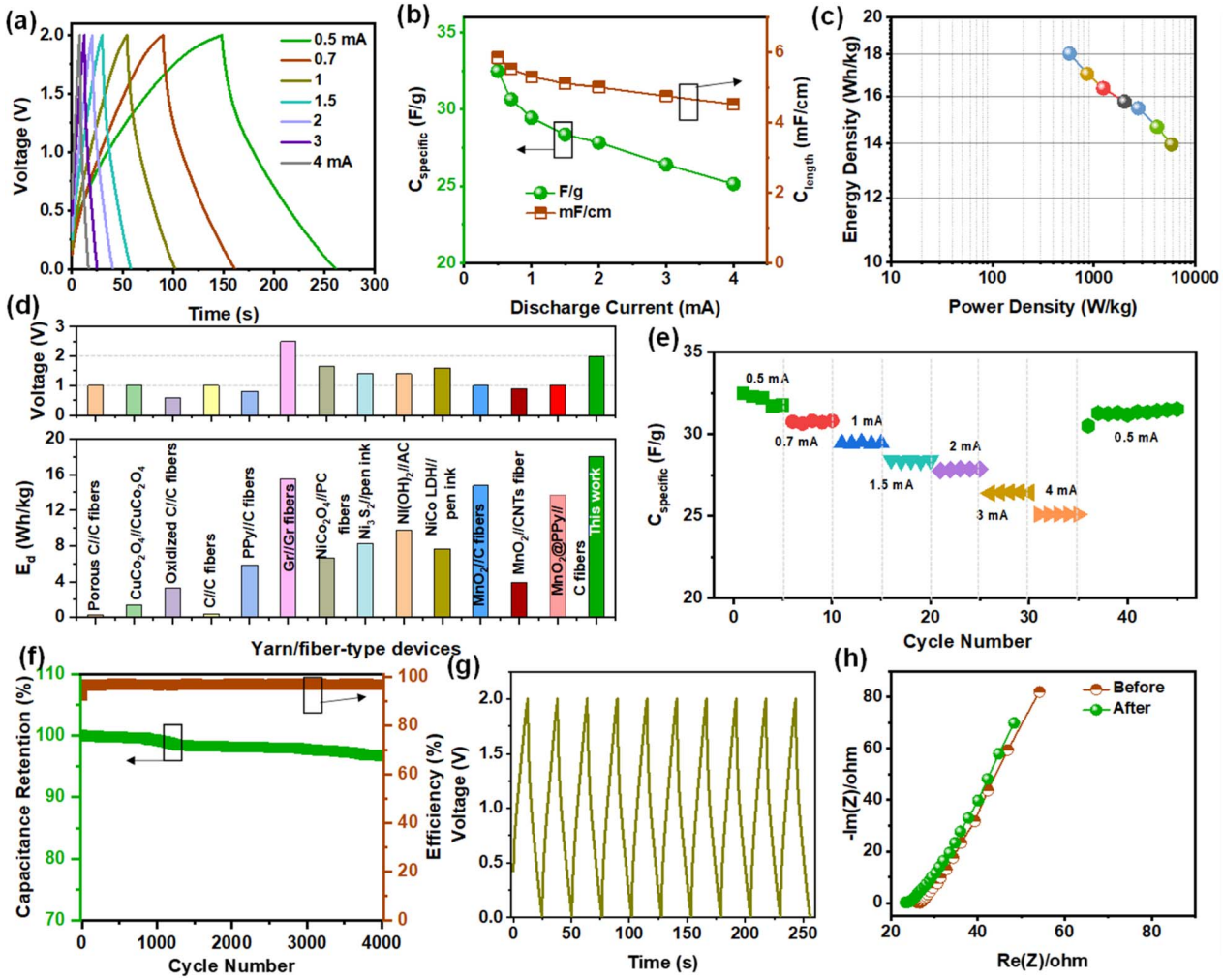

Fig. 6 (a) GCD curves, (b) calculated specific/length capacitance *vs.* discharge currents, (c) Ragone plot of bundled fiber-type Na–MnO_2@CFBs//PFAC@CFBs device analyzed using different charge–discharge currents of 0.3–4 mA, (d) comparative voltage response and energy density of previously published asymmetric/symmetric SCs with our fiber-type ASC. (e) Rate capability *vs.* cycle number of our ASC measured at various discharge currents. (f) Cycling stability, (g) first ten GCD cycles and (h) Nyquist plots of the fabricated device before and after cycling test.

calculated.[38] Length capacitance is desirable for comparing energy storage performance in elongated and flexible energy storage devices. The Na–MnO_2@CFBs//PFAC@CFBs device exhibited a high-rate capability of ~77.2%. Specifically, the device exhibited a specific capacitance of 32.5 F g^{-1} and a length capacitance of 5.8 mF cm^{-1} at a discharge current of 0.5 mA, and these values were still maintained to be 25.1 F g^{-1} and 4.5 mF cm^{-1} when the current increased to 4 mA, which indicates high electrochemical performance. A Ragone plot illustrating the energy-power density relationship of the ASC device is presented in Fig. 6(c). The device exhibited a maximum energy density of 18.04 W h kg^{-1} at a power density of 575.7 W kg^{-1} and these values were retained as 14 W h kg^{-1} at a high-power density of 5829.1 W kg^{-1}, respectively. The high-energy storage properties of our bundled fiber-type ASC were compared with previously reported fiber-type, yarn-type, and wire-shaped SCs, as presented in Table S2† and Fig. 6(d). Evidently, our device showed a wider voltage of 2 V and high-energy density than most of the previously reported devices, including porous C//C fibers (1 V; 0.31 W h kg^{-1}),[39] $CuCo_2O_4$//$CuCo_2O_4$ (1 V; 1.42 W h kg^{-1}),[40] oxidized C//C fibers (0.6 V; 3.3 W h kg^{-1}),[41] C//C fibers (1 V; 0.386 W h kg^{-1}),[42] PPy//C fibers (0.8 V; 5.87 W h kg^{-1}),[43] Gr//Gr fibers (2.5 V; 15.5 W h kg^{-1}),[44] $NiCo_2O_4$//PC fibers (1.65 V; 6.61 W h kg^{-1}),[45] Ni_3S_2//pen ink (1.4 V; 8.2 W h kg^{-1}),[46] $Ni(OH)_2$//AC (1.4 V; 9.8 W h kg^{-1}),[47] NiCo LDH//pen ink (1.6 V; 7.66 W h kg^{-1}),[48] MnO_2//C fibers (1 V; 14.77 W h kg^{-1}),[49] MnO_2//CNTs fiber (0.9 V; 3.88 W h kg^{-1}),[50] and MnO_2@PPy//C fibers (1 V; 13.68 W h kg^{-1}).[51] These high-energy storage properties of our ASC device suggest that it has enormous potential for portable electronic applications. Moreover, the ASC device showed good capacitance retention of 88% after 4000 GCD cycles with high coulombic efficiency of 96.5%, as shown in Fig. 6(f). For further reference of coulombic efficiency, ten consecutive cycles with symmetry in unique charge–discharge times were presented in Fig. 6(g). Fig. 6(h) shows the Nyquist plots of the ASC device before and after long-term cycles, which include bulk resistance (R_s) (resistance of current collector, and electrolyte), charge transfer resistance

(R_{ct}) (due to electron transport), interfacial resistance (due to *iR* drop), CPE (irregular structural morphology), and *W* is Warburg diffusion resistance. The intercept value at the *X*-axis of the semicircle is used to find the R_s value, which is 23 Ω for Na–MnO_2@CFBs//PFAC@CFBs before the cycling test, after the cycling test, it is 27 Ω. The low R_s value indicates the fast ion diffusion and allows efficient electron transport in the electrode surface.

The fabricated yarn-type flexible ASC devices were also used for powering electronic devices because of the device's feasible merits including high voltage and energy storage properties with adoptable functionalities. The practical viability of an integrated assembly depends on their voltage and power capabilities. A combination of two bundled fiber-type ASCs was employed to illustrate variations in voltage and charge response when combined in series configurations. The CV curves obtained at 50 mV s^{-1} for a single and two ASC devices coupled in series are displayed in Fig. 7(a). Compared to the single fiber-type ASC voltage (2 V), the extended cell voltage of 4 V was evidenced by the series connected bundled fiber-type ASC devices. Highly flexible energy storage devices that can bend in different directions are essential for portable electronic device applications. A series of CV evaluations under various bending positions were measured under a constant scan rate of 50 mV s^{-1} (Fig. 7(b)), which displayed nearly identical current response, and the device performance was stable under normal, flexed conditions (i–iii). Fig. 7(c) presents the schematic representation of two serially connected yarn-type ASC devices that were utilized for renewable energy harvesting and energy storage using solar cell modules. The integrated hybrid systems were assembled by connecting positive and negative terminals of solar panels to the series-connected two fiber-type ASCs (Fig. 7(c)). The solar-charged fiber-type ASC was then connected to the digital clock, which successfully powered up for a long time, indicating its feasibility for alkaline battery-free devices. The output voltage and power of the commercial solar cell were

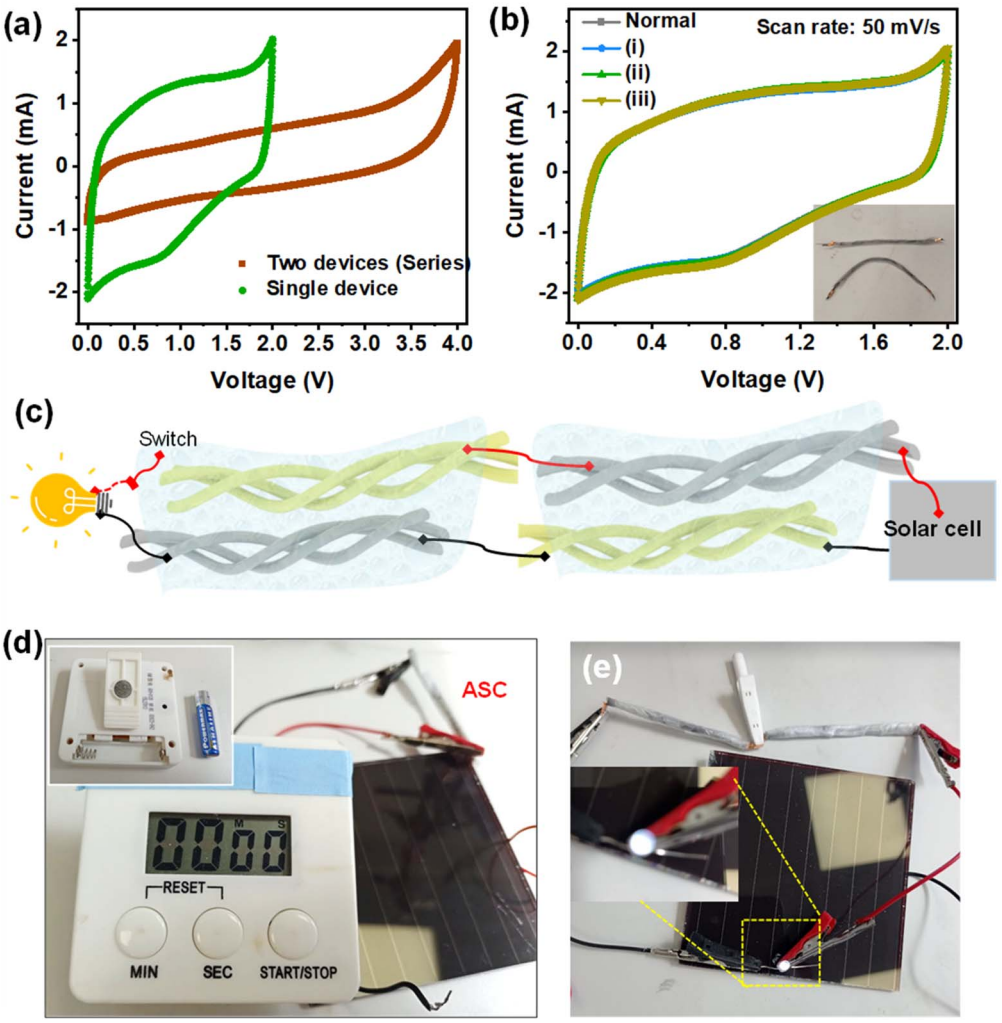

Fig. 7 (a) CV curves of the solitary and two-serially connected bundled fiber-type Na–MnO_2@CFBs//PFAC@CFBs devices showing the extended cell voltage of 4 V. (b) CV curves of the device measured under various flexed conditions. (c) Schematic diagram of integrated renewable energy conversion and storage using solar cell module and serially connected two fiber-type ASCs. (d and e) Practical applications of the solar charged ASCs powering the electronic display and white color light-emitting diode.

included in Fig. S5.† Moreover, the fiber-type ASCs were able to light up light-emitting diodes, which indicate the potential electronic applications of the fiber-type ASCs (Fig. 7(d and e)). Considering the superior electrochemical performance, core–shell Na–MnO_2 and biomass-derived porous carbon decorated bundled CFBs show prominence as flexible array electrodes for miniatured energy storage devices.

4. Conclusions

In conclusion, core–shell-type heterostructured Na–MnO_2 was facilely deposited on bundled carbon fibers (CFBs) by the simple, scalable, and facile electrodeposition method. Morphological and structural properties reveal that the effective intercalation of Na-ions in the layered structure of MnO_2 structures. When used as pseudocapacitive electrode, the core–shell Na–MnO_2@CFBs electrode showed better energy storage performance than the dense MnO_2@CFBs, owing to the increased interlayers, high electrochemical activity, and excellent electronic conductivity. At a discharge current of 0.3 mA, core–shell layered Na–MnO_2 showed a high specific capacitance of 222.5 F g^{-1} with excellent cycling stability. Moreover, a cost-effective PFAC was prepared by the biomass palmyra fruit shell waste, which showed a highly porous nature and good capacitive properties. Using the Na–MnO_2 and PFAC-based bundled fiber electrodes, the ASC device was fabricated, and the device demonstrated a maximum energy density of 18.04 W h kg^{-1} and a high-power density of 5829.1 W kg^{-1} with a high voltage of 2.0 V. The rational design of core–shell Na–MnO_2 using the electrochemical pre-intercalation appears to be a viable way to engineer hierarchical morphologies and accelerate the diffusion of electrolyte ions. A renewable-charging system was designed using a solar cell to show the switching proximity applications of integrated fiber-type ASC devices. The fiber-type ASC devices have the potential to energize light-emitting diodes and electronic portable displays after storing solar energy as renewable energy. These findings highlight the significant potential of pre-intercalated alkali-pseudocapacitive, and biomass-derived capacitive-electrodes towards enhanced energy storage performance and introduce a novel concept of bundled fiber-type devices for miniatured electronic applications.

Data availability

Raw data supporting the study are available from the corresponding authors upon readers requests.

Conflicts of interest

There are no conflicts to declare.

Acknowledgements

This work was also supported by the National Research Foundation (NRF) of Korea funded by the Korean government with grant NRF-2019R1A5A8080290 and RS-2023-00280665.

References

1 J. A. Lee, M. K. Shin, S. H. Kim, H. U. Cho, G. M. Spinks, G. G. Wallace, M. D. Lima, X. Lepró, M. E. Kozlov, R. H. Baughman and S. J. Kim, Ultrafast charge and discharge biscrolled yarn supercapacitors for textiles and microdevices, *Nat. Commun.*, 2013, **4**, 1970, DOI: 10.1038/ncomms2970.

2 L. Li, Z. Lou, D. Chen, K. Jiang, W. Han and G. Shen, Recent Advances in Flexible/Stretchable Supercapacitors for Wearable Electronics, *Small*, 2018, **14**, 1702829, DOI: 10.1002/smll.201702829.

3 J. He, L. Cao, J. Cui, G. Fu, R. Jiang, X. Xu and C. Guan, Flexible Energy Storage Devices to Power the Future, *Adv. Mater.*, 2024, **36**, 2306090, DOI: 10.1002/adma.202306090.

4 Poonam, K. Sharma, A. Arora and S. K. Tripathi, Review of supercapacitors: Materials and devices, *J. Energy Storage*, 2019, **21**, 801–825, DOI: 10.1016/j.est.2019.01.010.

5 G. Nagaraju, S. C. Sekhar, B. Ramulu, S. J. Arbaz and J. S. Yu, Multicomponent architectured battery-type flexible yarns for high-performance wearable supercapatteries, *Chem. Eng. J.*, 2021, **411**, 128479, DOI: 10.1016/j.cej.2021.128479.

6 G. Nagaraju, S. C. Sekhar and J. S. Yu, Utilizing Waste Cable Wires for High-Performance Fiber-Based Hybrid Supercapacitors: An Effective Approach to Electronic-Waste Management, *Adv. Energy Mater.*, 2018, **8**, 1702201, DOI: 10.1002/aenm.201702201.

7 H. Hu, Z. Pei and C. Ye, Recent advances in designing and fabrication of planar micro-supercapacitors for on-chip energy storage, *Energy Storage Mater.*, 2015, **1**, 82–102, DOI: 10.1016/j.ensm.2015.08.005.

8 Y. Pathaare, A. M. Reddy, P. Sangrulkar, B. Kandasubramanian and A. Satapathy, Carbon hybrid nano-architectures as an efficient electrode material for supercapacitor applications, *Hybrid Adv.*, 2023, **3**, 100041, DOI: 10.1016/j.hybadv.2023.100041.

9 H. Li, H. Yang, H. Sun, Y. Huang, P. An, Y. Yunhua and H. Zhao, A manganese oxide/biomass porous carbon composite for high-performance supercapacitor electrodes, *Electrochim. Acta*, 2024, **473**, 143514, DOI: 10.1016/j.electacta.2023.143514.

10 D. Zhang, L. Miao, Z. Song, X. Zheng, Y. Lv, L. Gan and M. Liu, Electrolyte Additive Strategies for Safe and High-Performance Aqueous Zinc-Ion Batteries: A Mini-Review, *Energy Fuels*, 2024, **38**, 12510–12527, DOI: 10.1021/acs.energyfuels.4c02287.

11 Y. Chen, Z. Song, Y. Lv, L. Gan and M. Liu, NH^{4+}-Modulated Cathodic Interfacial Spatial Charge Redistribution for High-Performance Dual-Ion Capacitors, *Nano–Micro Lett.*, 2025, **17**, 117, DOI: 10.1007/s40820-025-01660-0.

12 X. Yang, C. Hu, Y. Chen, Z. Song, L. Miao, Y. Lv, H. Duan, M. Liu and L. Gan, Tailoring ion-accessible pores of robust nitrogen heteroatomic carbon nanoparticles for high-capacity and long-life Zn-ion storage, *J. Energy Storage*, 2024, **104**, 114509, DOI: 10.1016/j.est.2024.114509.

13 J. M. Lim, Y. S. Jang, H. V. T. Nguyen, J. S. Kim, Y. Yoon, B. J. Park, D. H. Seo, K.-K. Lee, Z. Han, K. (Ken) Ostrikov and S. G. Doo, Advances in high-voltage supercapacitors for energy storage systems: materials and electrolyte tailoring to implementation, *Nanoscale Adv.*, 2023, **5**, 615–626, DOI: **10.1039/D2NA00863G**.

14 J. Huang, Y. Xie, Y. You, J. Yuan, Q. Xu, H. Xie and Y. Chen, Rational Design of Electrode Materials for Advanced Supercapacitors: From Lab Research to Commercialization, *Adv. Funct. Mater.*, 2023, **33**, 2213095, DOI: **10.1002/adfm.202213095**.

15 I. Khan, N. Baig, S. Ali, M. Usman, S. A. Khan and K. Saeed, Progress in layered cathode and anode nanoarchitectures for charge storage devices: Challenges and future perspective, *Energy Storage Mater.*, 2021, **35**, 443–469, DOI: **10.1016/j.ensm.2020.11.033**.

16 S. K. Ghosh, Diversity in the Family of Manganese Oxides at the Nanoscale: From Fundamentals to Applications, *ACS Omega*, 2020, **5**, 25493–25504, DOI: **10.1021/acsomega.0c03455**.

17 S. Komaba, N. Kumagai and S. Chiba, Synthesis of layered MnO_2 by calcination of $KMnO_4$ for rechargeable lithium battery cathode, *Electrochim. Acta*, 2000, **46**, 31–37, DOI: **10.1016/S0013-4686(00)00535-1**.

18 Y. Liu, J. Xu, J. Li, Z. Yang, C. Huang, H. Yu, L. Zhang and J. Shu, Pre-intercalation chemistry of electrode materials in aqueous energy storage systems, *Coord. Chem. Rev.*, 2022, **460**, 214477, DOI: **10.1016/j.ccr.2022.214477**.

19 Y. Zhou, T. Chen, J. Zhang, Y. Liu and P. Ren, Amorphous MnO_2 as Cathode Material for Sodium-ion Batteries, *Chin. J. Chem.*, 2017, **35**, 1294–1298, DOI: **10.1002/cjoc.201600915**.

20 L. Mai, H. Li, Y. Zhao, L. Xu, X. Xu, Y. Luo, Z. Zhang, W. Ke, C. Niu and Q. Zhang, Fast Ionic Diffusion-Enabled Nanoflake Electrode by Spontaneous Electrochemical Pre-Intercalation for High-Performance Supercapacitor, *Sci. Rep.*, 2013, **3**, 1718, DOI: **10.1038/srep01718**.

21 S. Liu, C.-Z. Fan, Y. Zhang, C.-H. Li and X.-Z. You, *J. Power Sources*, 2011, **196**, 10502–10506.

22 A. A. Radhiyah, M. I. Izwan, V. Baiju, C. K. Feng, I. Jamil and R. Jose, Doubling of electrochemical parameters *via* the pre-intercalation of Na+ in layered MnO2 nanoflakes compared to α-MnO_2 nanorods, *RSC Adv.*, 2015, **5**, 9667–9673, DOI: **10.1039/C4RA15536J**.

23 A. Amiri, A. Bruno and A. A. Polycarpou, Configuration-dependent stretchable all-solid-state supercapacitors and hybrid supercapacitors, *Carbon Energy*, 2023, **5**, e320, DOI: **10.1002/cey2.320**.

24 C. Lu, H. Jiang, X. Cheng, J. He, Y. Long, Y. Chang, X. Gong, K. Zhang, J. Li, Z. Zhu, J. Wu, J. Wang, Y. Zheng, X. Shi, L. Ye, M. Liao, X. Sun, B. Wang, P. Chen, Y. Wang and H. Peng, High-performance fibre battery with polymer gel electrolyte, *Nature*, 2024, **629**, 86–91, DOI: **10.1038/s41586-024-07343-x**.

25 L. Liu, Y. Yu, C. Yan, K. Li and Z. Zheng, Wearable energy-dense and power-dense supercapacitor yarns enabled by scalable graphene–metallic textile composite electrodes, *Nat. Commun.*, 2015, **6**, 7260, DOI: **10.1038/ncomms8260**.

26 P. Lestari Handayani, T. Kim, Y. Hwa Song, J. Seo Park, S. Jae Yang and U. Hyeok Choi, Tailoring molecular interaction in heteronetwork polymer electrolytes for stretchable, high-voltage fiber supercapacitors, *Chem. Eng. J.*, 2023, **452**, 139432, DOI: **10.1016/j.cej.2022.139432**.

27 J. Ye, X. Ji, Z. Liu, K. Liu, J. Li, R. Wang, J. Wang and Q. Lei, Carbon fiber reinforced structural battery composites: Progress and challenges toward industrial application, *Composites, Part B*, 2024, **277**, 111411, DOI: **10.1016/j.compositesb.2024.111411**.

28 F. Zhang, P. C. Sherrell, W. Luo, J. Chen, W. Li, J. Yang and M. Zhu, Organic/Inorganic Hybrid Fibers: Controllable Architectures for Electrochemical Energy Applications, *Adv. Sci.*, 2021, **8**, 2102859, DOI: **10.1002/advs.202102859**.

29 A. Chowdhury, R. Shukla, K. Bhattacharyya, A. K. Tyagi, A. Chandra and V. Grover, Electrochemical performance of K^+ -intercalated MnO_2 nano-cauliflowers and their Na-ion-based pseudocapacitors, *Mater. Sci. Eng., B*, 2023, **295**, 116581, DOI: **10.1016/j.mseb.2023.116581**.

30 G. Brugnetti, C. Triolo, A. Massaro, I. Ostroman, N. Pianta, C. Ferrara, D. Sheptyakov, A. B. Muñoz-García, M. Pavone, S. Santangelo and R. Ruffo, Structural Evolution of Air-Exposed Layered Oxide Cathodes for Sodium-Ion Batteries: An Example of Ni-doped Na_xMnO_2, *Chem. Mater.*, 2023, **35**, 8440–8454, DOI: **10.1021/acs.chemmater.3c01196**.

31 V. Sannasi and K. Subbian, Influence of Moringa oleifera gum on two polymorphs synthesis of MnO2 and evaluation of the pseudo-capacitance activity, *J. Mater. Sci.: Mater. Electron.*, 2020, **31**, 17120–17132, DOI: **10.1007/s10854-020-04272-z**.

32 T. Gao, M. Glerup, F. Krumeich, R. Nesper, H. Fjellvåg and P. Norby, Microstructures and Spectroscopic Properties of Cryptomelane-type Manganese Dioxide Nanofibers, *J. Phys. Chem. C*, 2008, **112**, 13134–13140, DOI: **10.1021/jp804924f**.

33 R. A. Davoglio, G. Cabello, J. F. Marco and S. R. Biaggio, Synthesis and characterization of α-MnO_2 nanoneedles for electrochemical supercapacitors, *Electrochim. Acta*, 2018, **261**, 428–435, DOI: **10.1016/j.electacta.2017.12.118**.

34 K. Liu, S. Tan, J. Moon, C. J. Jafta, C. Li, T. Kobayashi, H. Lyu, C. A. Bridges, S. Men, W. Guo, Y. Sun, J. Zhang, M. P. Paranthaman, X.-G. Sun and S. Dai, Insights into the Enhanced Cycle and Rate Performances of the F-Substituted P2-Type Oxide Cathodes for Sodium-Ion Batteries, *Adv. Energy Mater.*, 2020, **10**, 2000135, DOI: **10.1002/aenm.202000135**.

35 V. Thapliyal, M. E. Alabdulkarim, D. R. Whelan, B. Mainali and J. L. Maxwell, A concise review of the Raman spectra of carbon allotropes, *Diamond Relat. Mater.*, 2022, **127**, 109180, DOI: **10.1016/j.diamond.2022.109180**.

36 A. C. Dassanayake, A. A. S. Gonçalves, J. Fox and M. Jaroniec, One-pot synthesis of activated porous graphitic carbon spheres with cobalt nanoparticles, *Colloids Surf., A*, 2019, **582**, 123884, DOI: **10.1016/j.colsurfa.2019.123884**.

37 M. R. Pallavolu, R. R. Nallapureddy, H. R. Goli, A. N. Banerjee, G. R. Reddy and S. W. Joo, Bioinspired tailoring of nanoarchitectured nickel sulfide@nickel permeated carbon composite as highly durable and redox

chemistry enabled battery-type electrode for hybrid supercapacitors, *J. Mater. Chem. A*, 2021, **9**, 25208–25219, DOI: **10.1039/D1TA08122E**.

38 G. K. Veerasubramani, K. Krishnamoorthy, P. Pazhamalai and S. J. Kim, Enhanced electrochemical performances of graphene based solid-state flexible cable type supercapacitor using redox mediated polymer gel electrolyte, *Carbon*, 2016, **105**, 638–648, DOI: **10.1016/j.carbon.2016.05.008**.

39 S. T. Senthilkumar and R. K. Selvan, Flexible Fiber Supercapacitor Using Biowaste-Derived Porous Carbon, *ChemElectroChem*, 2015, **2**, 1111–1116, DOI: **10.1002/celc.201500090**.

40 S. Gu, Z. Lou, X. Ma and G. Shen, $CuCo_2O_4$ Nanowires Grown on a Ni Wire for High-Performance, Flexible Fiber Supercapacitors, *ChemElectroChem*, 2015, **2**, 1042–1047, DOI: **10.1002/celc.201500020**.

41 W. Zhou, K. Zhou, X. Liu, R. Hu, H. Liu and S. Chen, Flexible wire-like all-carbon supercapacitors based on porous core–shell carbon fibers, *J. Mater. Chem. A*, 2014, **2**, 7250–7255, DOI: **10.1039/C3TA15280D**.

42 N. Lima, A. C. Baptista, B. M. M. Faustino, S. Taborda, A. Marques and I. Ferreira, Carbon threads sweat-based supercapacitors for electronic textiles, *Sci. Rep.*, 2020, **10**, 7703, DOI: **10.1038/s41598-020-64649-2**.

43 Y.-S. Sung and L.-Y. Lin, Systematic Design of Polypyrrole/Carbon Fiber Electrodes for Efficient Flexible Fiber-Type Solid-State Supercapacitors, *Nanomaterials*, 2020, **10**, 248, DOI: **10.3390/nano10020248**.

44 X. Zhao, B. Zheng, T. Huang and C. Gao, Graphene-based single fiber supercapacitor with a coaxial structure, *Nanoscale*, 2015, **7**, 9399–9404, DOI: **10.1039/C5NR01737H**.

45 S. T. Senthilkumar, N. Fu, Y. Liu, Y. Wang, L. Zhou and H. Huang, Flexible fiber hybrid supercapacitor with $NiCo_2O_4$ nanograss@carbon fiber and bio-waste derived high surface area porous carbon, *Electrochim. Acta*, 2016, **211**, 411–419, DOI: **10.1016/j.electacta.2016.06.059**.

46 J. Wen, S. Li, K. Zhou, Z. Song, B. Li, Z. Chen, T. Chen, Y. Guo and G. Fang, Flexible coaxial-type fiber solid-state asymmetrical supercapacitor based on Ni_3S_2 nanorod array and pen ink electrodes, *J. Power Sources*, 2016, **324**, 325–333, DOI: **10.1016/j.jpowsour.2016.05.087**.

47 S. T. Senthilkumar and R. K. Selvan, Fabrication and performance studies of a cable-type flexible asymmetric supercapacitor, *Phys. Chem. Chem. Phys.*, 2014, **16**, 15692–15698, DOI: **10.1039/C4CP00955J**.

48 L. Gao, J. U. Surjadi, K. Cao, H. Zhang, P. Li, S. Xu, C. Jiang, J. Song, D. Sun and Y. Lu, Flexible Fiber-Shaped Supercapacitor Based on Nickel–Cobalt Double Hydroxide and Pen Ink Electrodes on Metallized Carbon Fiber, *ACS Appl. Mater. Interfaces*, 2017, **9**, 5409–5418, DOI: **10.1021/acsami.6b16101**.

49 C. Guo, H. Ma, Q. Zhang, M. Li, H. Jiang, C. Chen, S. Wang and D. Min, Nano MnO_2 Radially Grown on Lignin-Based Carbon Fiber by One-Step Solution Reaction for Supercapacitors with High Performance, *Nanomaterials*, 2020, **10**, 594, DOI: **10.3390/nano10030594**.

50 T. Wang, D. Song, H. Zhao, J. Chen, C. Zhao, L. Chen, W. Chen, J. Zhou and E. Xie, Facilitated transport channels in carbon nanotube/carbon nanofiber hierarchical composites decorated with manganese dioxide for flexible supercapacitors, *J. Power Sources*, 2015, **274**, 709–717, DOI: **10.1016/j.jpowsour.2014.10.102**.

51 M. A. A. Mohd Abdah, N. Mohammed Modawe Aldris Edris, S. Kulandaivalu, N. Abdul Rahman and Y. Sulaiman, Supercapacitor with superior electrochemical properties derived from symmetrical manganese oxide-carbon fiber coated with polypyrrole, *Int. J. Hydrogen Energy*, 2018, **43**, 17328–17337, DOI: **10.1016/j.ijhydene.2018.07.093**.